

---

# GENERATION OF GIANT SOAP FILMS

---

✉ Marina Pasquet<sup>1</sup>, ✉ Frédéric Restagno<sup>1</sup>, ✉ Isabelle Cantat<sup>2</sup>, ✉ Emmanuelle Rio<sup>1</sup>,

<sup>1</sup> Université Paris-Saclay, CNRS, Laboratoire de Physique des Solides, 91405, Orsay, France.

<sup>2</sup> Université de Rennes, CNRS, IPR (Institut de Physique de Rennes) - UMR 6251, 35000 Rennes, France.

March 9, 2025

## ABSTRACT

Artists regularly make soap bubbles several meters long. In this article we make soap films up to two meters high by pulling a horizontal fishing line driven by belts out of a soapy solution at velocities ranging from 20 cm/s to 250 cm/s. We characterize the thickness profile of the central part of the film that behaves like a rubber band under tension. We show that its thickness profile is well described by a static model in which a homogeneous elastic film is stretched by its own weight. This leads to an exponential thickness profile with a characteristic length given by a competition between gravity and surface elasticity. The prefactor is fixed by the shape and area of the film, governed by the fishing line motion but also by a continuous extraction of foam film from the lateral menisci, thicker than the central part, and that progressively invades the film from its lateral boundaries. The model we propose captures the subtle interplay between gravity, film elasticity and film extraction and leads to predictions in good agreement with our experimental data.

## 1 Introduction

Bubble artists are able to create giant soap bubbles and films, *i.e.* larger than one meter, on a daily basis in their artistic performances. One example is Graeme Denton's world record for the largest vertical soap bubble exceeding 10 m in height, generated by pulling a ring out of a bath containing a soap solution at a velocity of about three meters per second Denton [2020]. In the artistic field, these records are regularly broken and this one dates from 2020. From a fundamental point of view, the existence of these giant objects raises many questions that are still to be elucidated, such as what limits this maximum size, the role of the entrainment velocity to make them, or even what sets the thickness profile of these giant films. Inspired by these ephemeral giant objects, we studied the generation of planar soap films up to two meters in size.

In the literature, soap films of comparable size are always fed from above Ballet and Graner [2006], Kellay and Goldburg [2002], Kellay [2017], Rutgers et al. [2001], Sane et al. [2018], Salkin et al. [2016], Kim and Mandre [2017]. Therefore we have developed a new experimental setup, presented in detail in a previous article Mariot et al. [2021]. The principle of the film generation is identical to what has been developed to study small soap films Lioni-Addad and Di Meglio [1992], Cohen-Addad and di Meglio [1994], Adelizzi and Troian [2004], Berg et al. [2005], Saulnier et al. [2011, 2014], Seiwert et al. [2017], Champougny et al. [2018] up to 10 cm: a frame made by a fishing line is pulled out of a bath at a controlled velocity and drags a soap film. At the small velocities (up to 10 cm/s) usually used in such experiments, the thickness at the bottom of the films  $h_{Fr}$  is given by a balance between viscous stress and capillarity and follows Frankel's law Mysels et al. [1959]:

$$h_{Fr} = 1,89 \ell_c Ca^{2/3} \quad (1)$$

where  $\ell_c = \sqrt{\gamma_0/(\rho g)}$  is the capillary length and  $Ca = \eta V/\gamma_0$  the capillary number.  $\gamma_0$  is the surface tension of the solution,  $\rho$  its density,  $\eta$  its viscosity,  $g$  the gravitational acceleration constant and  $V$  the entrainment velocity. The good agreement between this law and experimental data has been studied extensively as well as the deviations observed with complex fluids [Cohen-Addad and di Meglio, 1994], at high velocities [Berg et al., 2005, Seiwert et al., 2014a, Champougny et al., 2015] or at the top of the film [Saulnier et al., 2011].

During the film generation, the fluid velocity is much smaller close to the bath than close to the top fishing line. This leads to a stretching of the film and to a dilution of surfactants at the interface. In the limit of poorly soluble surfactants,

the creation of the film surface area leads to a diminution of the surfactant concentration  $\Gamma$  and thus to a higher surface tension  $\gamma$ . As a consequence, the film behaves as an elastic membrane which pulls on its sides to relax towards its initial area and surface tension. Surface tension and surfactant surface concentration are linked by the Gibbs surface elasticity Gibbs [1928], Prins et al. [1967],

$$E = - \frac{\partial \gamma}{\partial \ln \Gamma}, \quad (2)$$

which quantifies the surface tension variation subsequent to a change in surface concentration. This results in a surface tension in the film higher than in the meniscus, where the tension is assumed to remain close to its equilibrium value  $\gamma_0$ . The interfacial stress denoted  $\gamma_0 + \Delta\gamma$  leads to the extraction of a film from the menisci, especially along the lateral ones Cantat [2013], Seiwert et al. [2014b]. The hydrodynamic laws in the vicinity of the meniscus impose a coupling between  $\Delta\gamma$ , the extracted film thickness and the extraction velocity. In the limit of high Gibbs modulus and in a steady state regime, this coupling is derived from the Frankel's law (Eq. 1) Mysels et al. [1959], Seiwert et al. [2014a], Cantat [2013]:

$$\Delta\gamma = 3.85 \gamma_0 \text{Ca}^{2/3} = 2.03 \gamma_0 \frac{h_{\text{Fr}}}{\ell_c} \quad (3)$$

A film element at a given altitude is stretched not only by the entrainment of the fishing line but also by the weight of the film underneath [Lucassen-Reynders, 1981, Couder, 1981, de Gennes, 2001]. This leads to an additional vertical gradient of surface tension in the film and therefore to a gradient of extraction velocity along the vertical meniscus. The main goal of this article is to measure the thickness profile in the central part of the film during its generation, and to predict its evolution with a model that takes into account these different effects.

In this article, we first present in the part 2 the setup used to generate giant vertical films (up to 2 m) by pulling a fishing line out of a liquid bath at high velocity (between 20 and 250 cm/s). Our experimental results obtained by visualization and spectrometry will be described in part 3 and we will propose an *in-situ* measurement of the surface tension gradient in a static film. The hydrostatic model, which predicts the film thickness profile and of the surface tension gradient is proposed in the part 4 together with a numerical resolution of the proposed model. A direct comparison with measurements will be presented at the end of the part 5.

## 2 Presentation of the Experimental Setup

The experimental setup for the generation of vertical soap films has been described previously Mariot et al. [2021] and we will only outline the main features here. The films are formed by pulling a fishing line (in fluorocarbon with a diameter of 0.74 mm) out of a glass container, as we can see in the Fig. 1. This wire is driven out of the soap solution by two transmissions toothed belts. These belts are themselves driven by two coupled stepping motors (SM56 3 18 J4.6 from Rosier Mecatronique) associated with pulleys. The motors were chosen in order to be able to control the velocity of the generation of the films between 20 and 250 cm/s. The maximum size of the films we can generate with this device is 2 m high and 70 cm wide.

The setup allows automatic detection of the presence of the films, by measuring the reflection of a white light by three photoresistances. In addition, thickness measurements are also possible using a UV-VIS spectrometer (Ocean Optics Nanocalc 2000) associated with an optical fiber of 400  $\mu\text{m}$  diameter. This spectrometer, placed at the center of the films in the  $y$  direction (as defined in Fig. 1), allows a measurement of the local thickness and can be moved on the whole height of the films. To control the humidity in the environment where the films are generated, we used two commercial humidifiers (one located at the bottom of the device, the other at the top of the chamber). The bottom humidifier (Okoia AH450) allows us to select the target humidity and the top humidifier (Bonaire BU1300W-I), whose flow rate is adjustable, allows us to have a more homogeneous humidity in the chamber, especially when we want to work in a very humid environment. In the following, the humidity is fixed at  $85 \pm 4 \%$ , so we will neglect evaporation. The temperature is measured throughout the experiments with a typical uncertainty of 0.1  $^\circ\text{C}$  and corresponds to the ambient temperature, which is about 22  $^\circ\text{C}$ .

To make direct visualizations of the soap films, we illuminate them thanks to a large white photo studio background paper (BD 129 Super White  $2.72 \times 11$  m), which serves as a light reflector for four halogen lamps. We made a hole in it to fit the wide-angle lens (Nikon AF-P DX 10-20 mm) of a camera (Nikon D7200).

For each experiment, we use 5 liters of soap solution made of 4 % dishwashing liquid (Fairy from Procter & Gamble, containing between 15 % and 30 % of anionic surfactants) with ultrapure water, with resistivity greater than 18.2  $\text{M}\Omega\cdot\text{cm}$ .

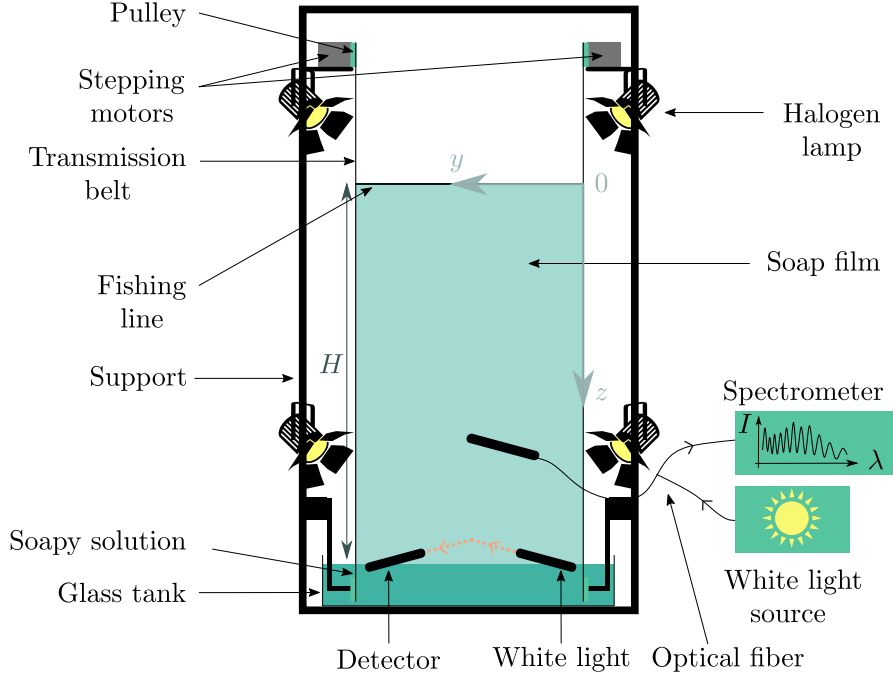


Figure 1: Schematic representation of the experimental setup allowing the generation of giant films.

### 3 Experimental characterization of giant soap films

In this section, we present experimental observations and thickness measurement data obtained using the experimental setup presented in part 2.

#### 3.1 Experimental observations

The qualitative behavior of the giant film during its generation is illustrated in Fig. 2, the interferential colors providing us a direct indication of the film thickness. We can see here that there is a central part (C) in which the film color is uniform at a given height, indicating a thickness stratification by the gravity. On the image on the left, on both sides of this central film we observe two lateral parts (F), which are thicker and not stratified. They correspond to the Frankel's films, extracted from the lateral menisci. The drawing of the boundaries in Fig. 2 was done by hand, under ImageJ. In the following, we will focus on the measure and prediction of the central film thickness profile. We will show that this necessitates a description of the lateral films extraction dynamics.

#### 3.2 Film thickness

Fig. 3 (a) shows the evolution of the thickness of a film entrained at a velocity of 60 cm/s as a function of time, for a spectrometer position fixed at 13 cm above the surface of the solution, at the center of the film (in the  $y$  direction). The time  $t = 0$  corresponds to the moment when the fishing line leaves the bath. We observe that up to  $t \simeq 1$  s there is a thinning of the central part of the film. After reaching a minimum value around  $1.2 \mu\text{m}$ , the thickness  $h$  increases linearly with time. This non-monotonic behavior is a robust phenomenon, as we can see in Fig. 3 (b), for all the measured velocities. We will show that this can be recovered by the model developed.

In Fig. 4, we have plotted these thicknesses as a function of the height  $H(t)$  reached by the films during the generation, *i.e.* as a function of the product  $V \times t$ , for two different spectrometer positions. This leads to a reasonable collapse of all the data on a master curve and a similar non-monotonic behavior is observed. The thickness evolution thus does not depend on the imposed velocity, which rules out inertial and air friction effects in the dynamics. The model will show

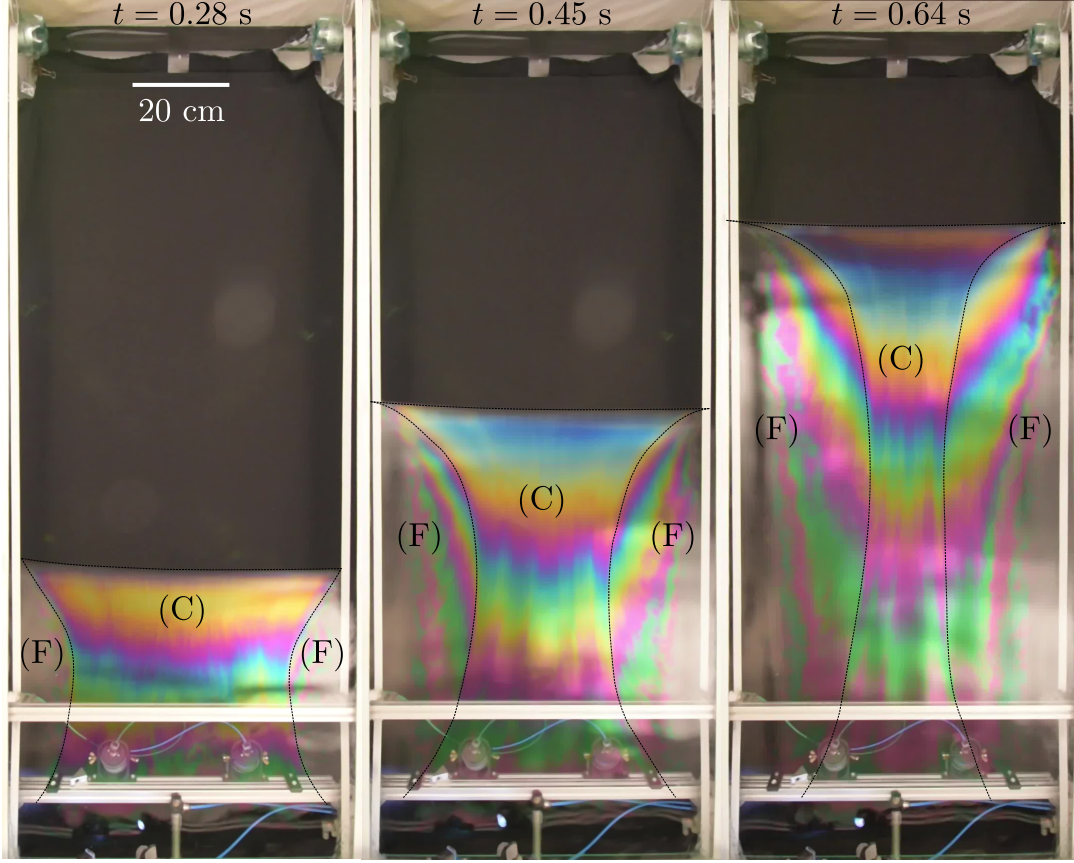


Figure 2: Photographs showing the evolution over time of a soap film generated at a fixed velocity of 200 cm/s. Thicker films extracted from the lateral menisci are observed: they are called Frankel films and are noted (F). The central film is noted (C).

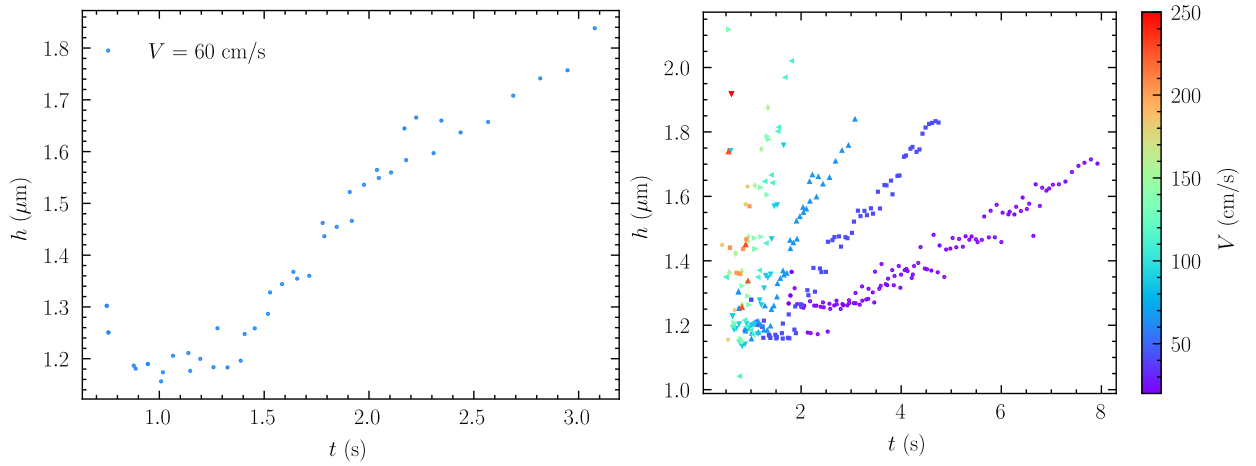


Figure 3: Evolution of the thickness  $h$  of soap films during the generation as a function of time  $t$ . These measurements were performed by spectrometry at the center of the films, at 13 cm above the surface of the bath. (a) Time evolution of the thickness for  $V = 60$  cm/s. (b) Time evolution of the thickness for all the velocities probed between 20 cm/s (purple) and 250 cm/s (red).

that the central film can indeed be described by a hydrostatic equilibrium, which can be disconcerting at first sight since we generate the films at high velocities.



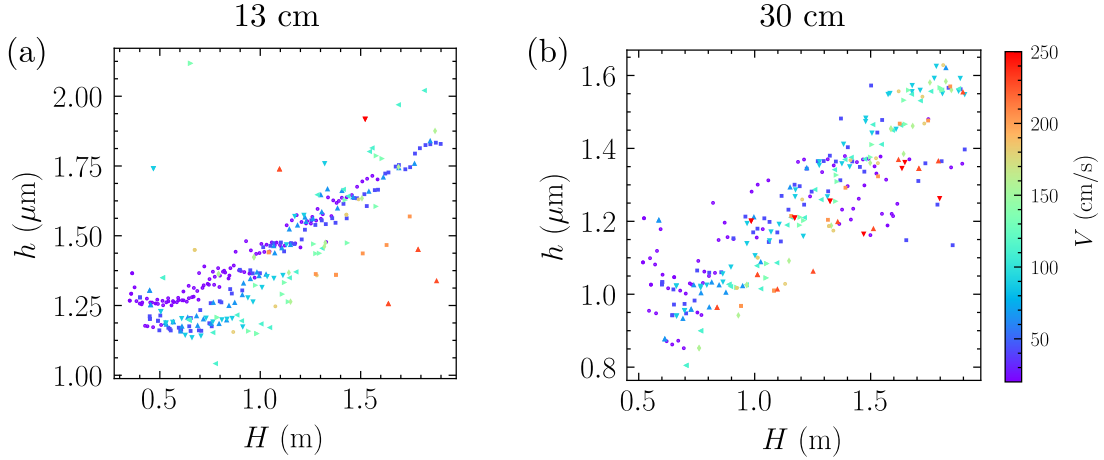


Figure 4: Evolution of the thickness  $h$  of the soap films during the generation as a function of the height  $H$  reached by the films, for all the velocities probed between 20 cm/s and 250 cm/s. These measurements are made by spectrometry (in the center of the films in the  $y$  direction) at 13 cm above the solution surface (a) and at 30 cm above the surface (b). In the figure (a), this is the same data as shown in Fig. 3 (b). With this type of representation, all the data are superimposed on the same master curve.

### 3.3 Film thickness profiles

We measured the thickness as a function of time for several positions of the spectrometer (between 3 and 180 cm above the liquid bath, in the center film in the  $y$  direction) in order to determine the whole film profile, in the central part of the film. These profiles are given for five successive times, and therefore for five different film heights, in Fig. 5 (a). Two zones can be identified, despite a limited spatial resolution due to the difficulty of the thickness measurement in films moving at high velocity. At small  $z$ , close to the top of the film (white background in Fig. 5 (a)), the profile can be fitted with an exponential model, whereas at large  $z$ , close to the liquid bath (gray background), the thickness is systematically larger than the extrapolation of this exponential profile. In the following, the exponential part will be referred to as the initial film. Indeed, at short time, a small quantity of liquid is entrained by the fishing line and forms an initial film. As we will see later, this initial film is a closed system, which is stretched by the fishing line movement and by the film weight. The physical process governing this initial film extraction seems to differ from the visco-capillary law (Eq. (1)) relevant at larger times.

The measurements made for seven entrained velocities, ranging from 20 cm/s to 140 cm/s, lead to the same results. The top part of the profiles have been fitted by the law

$$h(z) = K e^{(z-H)/\ell} \quad (4)$$

with  $\ell$  a characteristic length and  $K$  a prefactor. These lengths are plotted in Fig. 5 (b) as a function of the film height (during the film generation). The values of  $\ell$  obtained suggest that the characteristic length remains constant during the film's generation and does not depend on the entrained velocity. Taking into account all the experiments, we measure a characteristic length  $\ell = 0.80 \pm 0.09$  m.

In the following (part 4) we will develop a hydrostatic theoretical description of the films during their generation to rationalize these observations.

### 3.4 Area of lateral Frankel films

We determined the area  $A_{Fr}$  of the lateral Frankel's films by direct visualization, by dividing the films as described in the section 3.1. The ratio between  $A_{Fr}$  ( $A_{Fr}$  takes into account both sides of the film) and the total area  $A$  of the film is given as a function of the film height  $H$  for three different velocities in Fig. 6. This ratio, like the central film thickness, is governed by the film height and is independent of the entrained velocity.

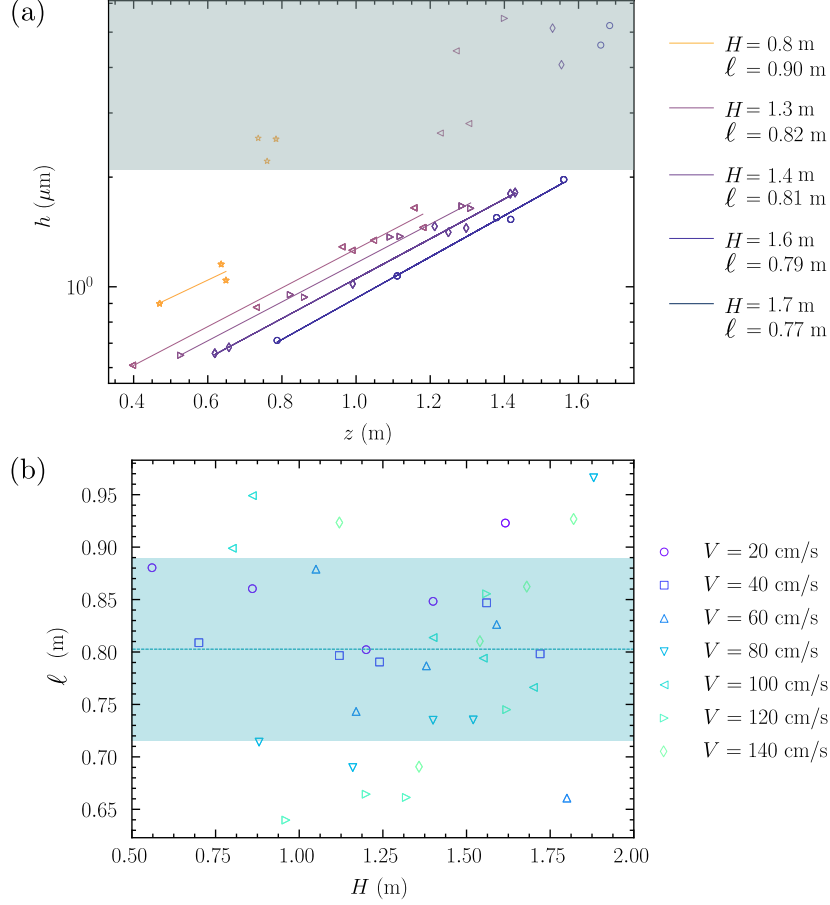


Figure 5: (a) Thickness  $h$  of the soap films measured during the generation as a function of  $z$  (oriented downwards, with the origin at the top of the film), in semi-logarithmic scale, for a velocity fixed at 100 cm/s. For a given instant, corresponding to a color, the value of  $\ell$  extracted from the exponential fit and the height of the films  $H$  are written in the legend. The average value is  $\ell \simeq 0.82$  m. The points at the bottom of the films (3 cm from the bath) not described by the exponential are shown in the grayed area. (b) Measurement of the characteristic length  $\ell$  on the thickness profiles for different velocities (ranging from 20 cm/s to 140 cm/s). The values of  $\ell$  are plotted as a function of the height reached by the soap  $H$  films during this generation. The average value of  $\ell$  measured for all the probed velocities is indicated by a blue line. The experimentally determined standard deviation is represented by the colored rectangle. All our measurements lead to  $\ell = 0.80 \pm 0.09$  m.

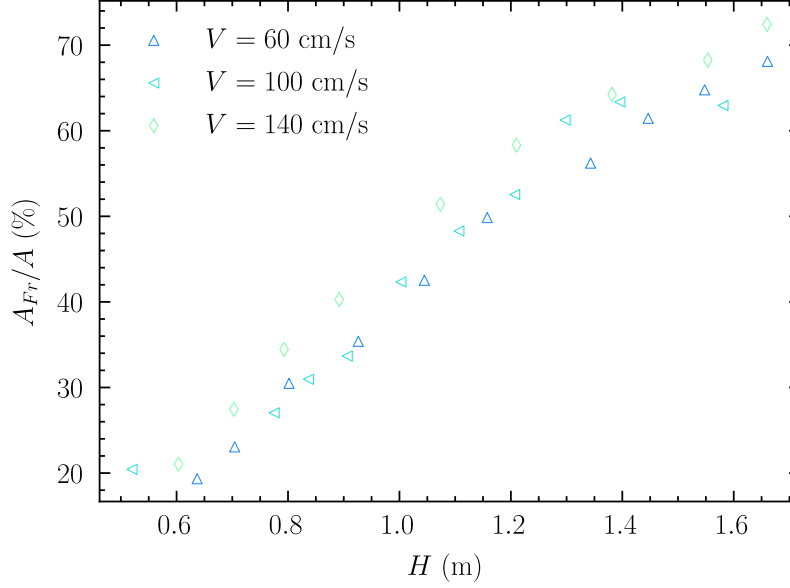


Figure 6: Evolution of the proportion of the area of the lateral Frankel films  $A_{Fr}$  to the total area of the films  $A$  as a function of the height  $H$  reached by the soap films during their generation for three different velocities: 60 cm/s, 100 cm/s and 140 cm/s.

### 3.5 Surface tension gradients in the films

As explained in the introduction, a vertical surface tension gradient due to gravity is expected along the giant soap film, which we propose to measure in this section. We perform this measurement for a static (i.e., after the generation) soap film of 120 cm high.

The surface tension is deduced from the deformation of a small elastic object, put at different heights in the film. This method was initially proposed by Adami *et al.* [Adami and Caps, 2015], and used in 15 cm high fed films.

The elastic object used for the measure is shown in Fig. 7 (a). The sensor is made with Silicone SKIN FX 10 (from Rougier & Pl  ), using a PTFE mold (see Fig. 7 (b)). This matter is usually used to make prosthesis or special effects in movies, and makes it possible to manufacture elastic objects in less than an hour.

The obtained sensor is held at the chosen height in the plane of the film by a thin wire attached to the horizontal fishing line entraining the films, and the piece of film trapped inside is pierced to perform the measure. The unbalanced tension forces outside the object deform the arms, as its shape tends to get closer to a circle. This deformation is quantified by the distance  $\delta$  defined in Fig. 7 (a). The deformation  $\delta$  varies linearly with the tension around the object [Adami and Caps, 2015]:

$$\gamma = \frac{16e^4 E}{l^4} \delta \quad (5)$$

with  $e$  the thickness of the arms of the elastic object ( $e = 0.8$  mm),  $E$  the Young's modulus of the object ( $E \simeq 0.4$  MPa) and  $l$  the height of the arms ( $l = 24$  mm). As the Young modulus of the object is not precisely known, the prefactor of the linear relation (5) is obtained from a calibration with horizontal soap films of known surface tension: a solution containing TTAB at a concentration of 10 cmc ( $\gamma = 39$  mN/m), a solution containing Fairy diluted to 4 % ( $\gamma = 25.2$  mN/m) and a solution containing Tween 20 at 1 % ( $\gamma = 33.7$  mN/m).

From an experimental point of view, this measurement is a real challenge because the films last only a few seconds.

The results obtained for a 120 cm high static film, entrained at a velocity of 100 cm/s, are shown in Fig. 7 (c). The measurements begin just after the motors stop, and last 10 seconds. The thicknesses given in the inset are average during this time period. We measure a surface tension difference, between the top and bottom of the film, of about 5 mN/m, which we will compare to a theoretical prediction in the next paragraph.

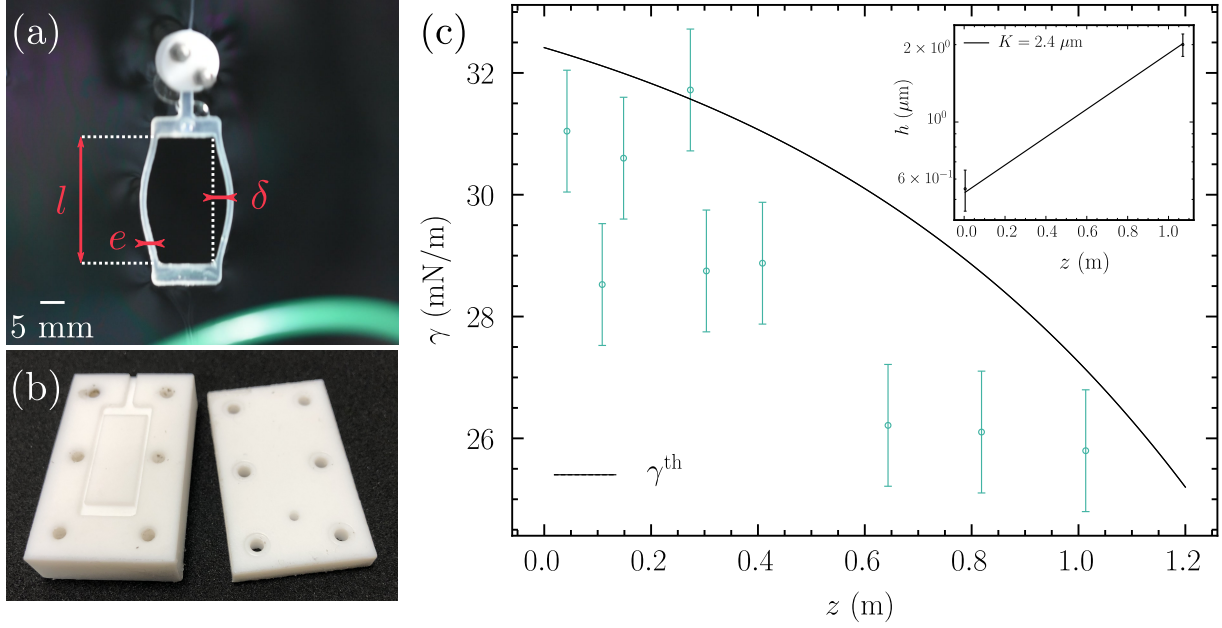


Figure 7: (a) Example of an image recorded during an experiment. The arms of the elastic object are deformed due to the surface tension forces. (b) Photograph of the PTFE mold used to fabricate the elastic object. (c) Surface tension  $\gamma$  measured at the center (in the  $y$  direction) of a film of height  $H=120$  cm as a function of the coordinate  $z$ , just after the motors stop. The black line corresponds to the surface tension  $\gamma^{\text{th}}$ , obtained by integrating Eq. (6) using the film thickness profile given in inset, with the equilibrium tension at the film bottom. Inset: film thickness obtained by spectrometry at two different high. The whole profile (black line) is the prediction of Eq. (4) with  $\ell = 0.8$  m taken from Fig. 5 and  $K = 2.4 \mu\text{m}$  as adjustable parameter.

## 4 Theoretical description of the soap films during their generation

### 4.1 Equilibrium film thickness profile under gravity

A static model build by Lucassen [Lucassen-Reynders, 1981] and used by de Gennes [de Gennes, 2001] relies on the fact that the weight of the soap films is balanced by the surface tension gradient so that

$$\rho gh + 2 \frac{\partial \gamma}{\partial z} = 0, \quad (6)$$

with  $h$  the thickness of the soap film and with the vertical axis  $z$  oriented downwards.

This equation is simply a force balance in the vertical direction, per unit area, on a film element of volume  $dV = h dA$  spanning from one interface to the other.

The validity of Eq. (6) can be tested using the tension measurements made in 120 cm high static film, described in the section 3.5. To obtain the theoretical profile shown in Fig. 7 (c), inset, we assumed an exponential variation of the thickness with  $z$ . The measurements are compatible with the characteristic length  $\ell = 0.8$  m, as obtained for all films during generation (see Fig. 5). The theoretical tension profile is then obtained by integration of Eq. (6), using the theoretical profile and  $\gamma_0 = 25.2$  mN/m,  $\rho = 997$  kg/m<sup>3</sup> and  $g = 9.81$  m/s<sup>2</sup>. The measure, shown in Fig. 7 (c), is slightly below the prediction proposed, but with an agreement close to the experimental uncertainty.

The surface tension involved in Eq. (6) depends on the interface surfactant concentration  $\Gamma$ . For small coverage variations, an interface elasticity  $E$  is defined by Eq. (2) and a linearized expression of the surface tension can be expressed as  $\gamma = \gamma_0 - E(\Gamma - \Gamma_0)/\Gamma_0$ .

Here, we will focus on films stabilized by a dishwashing liquid and we will assume that the film elasticity is mainly due to poorly soluble surfactant molecules, of negligible bulk concentration. In that case, a simple relationship between  $E$  and the film mechanical dilatational elasticity, *i.e.* between the film tension and dilatation or compression can be obtained, once the reference state of each film element is defined.

In this aim, we consider a film element of volume  $dV$  and define its reference state, indicated by the subscript 0, as the state in which the interface concentration is in equilibrium with the bulk liquid used to produce the film. It is characterized by its area  $dA_0$ , its thickness  $h_0$  and the interface concentration  $\Gamma_0$ . The relative motion of the bulk phase with respect to the interfaces is a downwards Poiseuille flow, with a velocity scaling as  $\rho g h^2 / \eta \sim 10 \mu\text{m/s}$ , which is entirely negligible in our experiment. A film element is thus a closed material system. Consequently, when the film element is stretched to reach an area  $dA$ , the volume conservation imposes  $h dA = h_0 dA_0$ . Moreover, the surfactant conservation leads to  $h\Gamma = h_0\Gamma_0$  and finally

$$\gamma = \gamma_0 + E \frac{\varepsilon}{1 + \varepsilon} \quad (7)$$

with the extension  $\varepsilon$  defined by :

$$\varepsilon = \frac{dA}{dA_0} - 1 = \frac{h_0}{h} - 1. \quad (8)$$

As there are two interfaces, the film tension is simply  $2\gamma$ .

From these relations, we get  $\partial_z \gamma = E \partial_z (h/h_0)$ , and Eq. 6 becomes

$$\frac{1}{h} \frac{\partial}{\partial z} \left( \frac{h}{h_0} \right) = \frac{\rho g}{2E}. \quad (9)$$

In the case of soluble surface-active molecules, the film elasticity also depends on the film thickness Prins et al. [1967], Van den Tempel et al. [1965], Lucassen-Reynders [1981]. In the frame of this model, the thickness profile of the soap film is a 2D equivalent of a 3D compressible gas in a gravity field.

The Eq. (9) governs the thickness profile of a film in a gravity field. It predicts an exponential profile only if the reference thickness  $h_0$  does not vary with the position  $z$ . Indeed, in this case it can be integrated to get

$$h(z) = h(H) e^{(z-H)/\ell} \quad \text{with} \quad \ell = \frac{2E}{\rho g h_0} \quad (10)$$

the characteristic length of the problem. The exponential profile observed in Fig. 5 is thus the signature of a homogeneous reference thickness in the initial film.

This reference thickness is governed by the amount of surfactant trapped in the film during its extraction. As it is constant in the upper part of the film (defined as the initial film), its value does not depend on time during the first moment of the film extraction. Even more surprisingly, it does not depend on the motors' velocity. This is an important experimental result that we have not been able to elucidate yet, as discuss in the conclusion.

Indeed, as verified in Fig. 5 (b), the characteristic length  $\ell$  is constant with time, which is consistent with the fact that a film element is a closed material system, keeping the same reference thickness at all times.

In order to determine the thickness profile  $h(z)$  completely, it still remains to determine the value of the thickness  $h(H)$ . We will show that it only depends on the area and on the shape of the initial film.

## 4.2 Validity of the equilibrium force balance

The Eq. (6) is the projection in the vertical direction of the vectorial equilibrium condition of the film  $\rho g h \vec{e}_z + 2 \vec{\nabla} \gamma = 0$ . Taking the curl of this equation, we obtain  $\partial_y \gamma = 0$ , with  $y$  the horizontal direction in the film plane. Now using  $\rho g h = -2 \partial_z \gamma$  we obtain, after a derivation, the condition  $\partial_y h = 0$ . This condition is verified in the central part of the film, but not in the lateral part, which is thus necessary in an out of equilibrium situation (see Fig. 2).

The air friction on a moving film can be estimated using the Prandtl theory Rutgers et al. [1996]. It scales as  $\eta_a V / \delta_{BL}$  with the boundary layer thickness  $\delta_{BL} \sim [\eta_a H / (\rho_a V)]^{1/2}$ , the air viscosity  $\eta_a = 1.8 \text{ kg/m/s}$ , the air density  $\rho_a = 1.3 \text{ kg/m}^3$ , and the film height  $H \sim 1 \text{ m}$ . In the initial film, the velocity varies from the motors' velocity at the top to a much smaller velocity at the bottom (as will be shown later). For the smallest motors' velocity,  $V = 0.2 \text{ m/s}$ , the air friction is thus at most of the order of  $10^{-3} \text{ kg m}^{-1} \text{ s}^{-2}$  and should be negligible in comparison with the gravity of the order  $\rho g h \sim 10^{-2} \text{ kg m}^{-1} \text{ s}^{-2}$ . The highest motor velocities are close to the terminal velocities observed for films of comparable thickness (see Fig. 4 in Rutgers et al. [1996]) and air friction should begin to play a significant role. However, the rescaling obtained in Fig. 4 shows that the influence of the motors' velocity is small, and the air friction will be neglected in the model. The inertia of the central film scales as  $\rho h V^2 / H \sim 10^{-3} \text{ kg m}^{-1} \text{ s}^{-2}$  and will be neglected too.

Finally, the surface shear viscosity leads to an in-plane friction force of the order of  $\eta_s \delta V / L^2$ , with  $\delta V$  a velocity difference between two points of the film separated from a distance  $L$  and  $\eta_s \sim 10^{-7} - 10^{-6}$  kg/s Stevenson [2005] the shear interface viscosity. The thickness stratification in the central part of the film indicates a uniform velocity in the  $y$  direction, and this viscous friction does not contribute to the force balance. The extracted films on the two film sides are thicker than the central part and fall down under gravity. If the downward velocity  $V^{\text{Fr}}$  reaches 1 m/s, with a characteristic width  $L = w^{\text{Fr}} \sim 10^{-1}$  m we get an upward viscous term of the order of  $10^{-4}$  kg m $^{-1}$  s $^{-2}$  in the Frankel film, which is negligible. The higher gravitational force in this thick part of the film is thus probably compensated by the film inertia.

On the basis of the previous discussion and of the observed rescaling in Fig. 4, the dynamics of the initial film will be rationalized using the equilibrium model of section 4.1. The modelization of the Frankel film motion is beyond the scope of this paper, and its downwards flow will be taken into account phenomenologically.

### 4.3 Modelization of the time evolution

The goal of this section is to predict the time evolution of the film thickness profile, on the basis of the model leading to Eq. (9). The thickness profile evolves because of the extraction of film from the menisci, which allows the relaxation of the initial film towards its reference thickness. Actually, this means that the area and shape of the initial film are the only ingredients to take into account.

We thus propose to describe completely the generation of soap films by taking into account the extraction of film from the menisci, at the bottom and on the lateral sides.

#### 4.3.1 Film parametrization and equilibrium equation

The central film is defined as the material system extracted from the bottom meniscus stretched by the fishing line entrainment. We assume that it remains invariant by translation in the horizontal direction, so the relevant elementary systems are horizontal film strips of homogeneous properties. These film elements are identified by their distance  $x$  from the top meniscus, measured in the reference state of the film, using a Lagrangian approach.  $x$  is the position the film element would have in the absence of gravity and with a film tension  $2\gamma_0$  imposed at its boundary (see Fig. 8). With this definition the film element of height  $dx$  is a closed material system, that is followed during its motion and deformation. This Lagrangian approach leads us to introduce the spatial variable  $\xi$  defined such that the position  $z$  of the tracked element in the film is related to the variable  $x$  via the relation :

$$z(x) = x + \xi(x) \quad (11)$$

The shape of the film element is a rectangle  $dx(1 + \partial_x \xi)w(x)$ , with  $w(x, t)$  the width of the central film, from one boundary with the lateral extracted film to the other. The reference thickness  $h_0(x)$  of the element of reference position  $x$  is determined by its extraction from the bath, which occurs at the time  $t^{\text{ex}}(x)$ . On the basis of our experimental results, it will be assumed uniform in the top part of the film, and then governed by the visco-capillary film extraction (Eq. (1)). Note that the Lagrangian variable  $x$  corresponds to a material system which keeps a reference thickness constant with time, so  $h_0$  may depend on  $x$  but not on time. The width of the element at  $t^{\text{ex}}(x)$  is  $w_0$ , as the film extraction occurs along the whole bottom meniscus length. This length is chosen as the reference width for the film element.

The volume  $dV$  of a film element is conserved during a deformation, which allows us to write

$$w_0 h_0(x) = (1 + \partial_x \xi) w(x) h(x). \quad (12)$$

Its area  $dA = w(x)(1 + \partial_x \xi)dx$  may in contrast vary and the film extension  $\epsilon(x)$  (Eq. (8)) is:

$$\epsilon(x) = \frac{w(x) (1 + \partial_x \xi)}{w_0} - 1 \quad (13)$$

Within the central part of the film, the force balance is given by Eq. (6) and (7) which becomes:

$$\rho g h(x) (1 + \partial_x \xi) = -2 E \partial_x \left( \frac{\epsilon(x)}{1 + \epsilon(x)} \right). \quad (14)$$

Using Eq. (12) we can reformulate this equation as a function of  $h_0$ ,  $w$  and  $\epsilon$  only

$$\partial_x \left( \frac{\epsilon(x)}{1 + \epsilon(x)} \right) = -\frac{1}{\ell} \frac{h_0(x)}{h_0} \frac{w_0}{w(x, t)}, \quad (15)$$



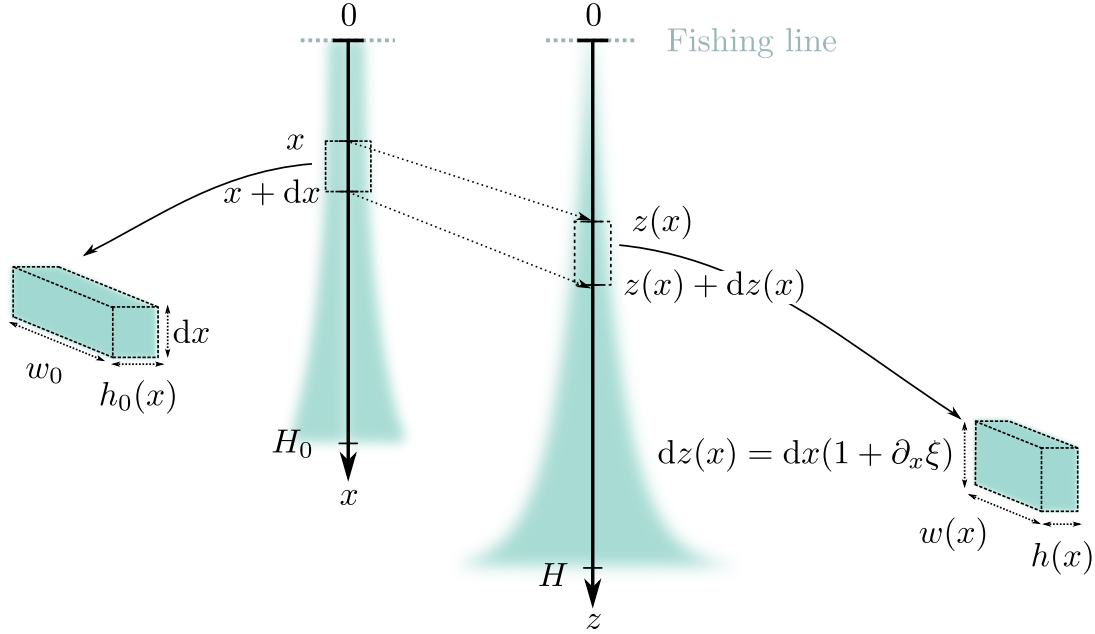


Figure 8: Scheme of the film profile and notations used in the text. (Left) Reference state of the film with a thickness  $h_0(x)$  and a height  $H_0$ . An elementary material system is defined between  $x$  and  $x + dx$ . (Right) Actual state of the film, in which the same elementary system is located between  $z(x)$  and  $z(x) + dz(x)$ .

with  $h_{00}$  an arbitrary reference and  $\ell = 2E/(\rho gh_{00})$  the characteristic length already defined in Eq. (10), (where  $h_{00}$  is taken as the uniform reference thickness  $h_0$  of Eq. (10)).

This determines the extension  $\epsilon$  and thus the whole film profile if the function  $w(x, t)$  and  $h_0(x)$  are known, as well as a boundary condition at the film bottom. These quantities are determined from the film extraction at the bottom and lateral menisci, and from the variation of the film height  $H$  imposed by the motors.

#### 4.3.2 Film extraction

In the limit of high film elastic modulus, and in a steady state regime, a film extraction at a velocity  $U_{Fr}$  is associated with a film tension  $2\gamma_0 + 2\Delta\gamma$  (Eq. (3)).

The extraction rate can thus be related to the local tension in the film, and using Eq. (7), to its deformation:

$$U_{Fr}(x) = \beta \left( \frac{\epsilon(x)}{1 + \epsilon(x)} \right)^{3/2} \quad \text{with} \quad \beta = k \frac{E^{3/2}}{\eta\gamma_0^{1/2}} \quad (16)$$

and  $k$  a numerical prefactor which theoretical value, deduced from Eq. (3), is  $k = 0.13$ .

The above equation assumes that the surface tension in the menisci is everywhere equal to the reference surface tension  $\gamma_0$ . This is a strong assumption, especially for the lateral menisci. If these menisci are not sufficiently effective surfactant reservoirs and become depleted, there can be a large error in the extraction velocity of the side films. To overcome this difficulty, we have chosen to use  $k$  as a fitting parameter. For the physical situation studied in this article, the theoretical prediction of  $\beta$  with the Eq. (16) is:  $\beta = 2.63$  m/s, with  $E = 22$  mN/m Kim and Mandre [2017], whereas the fitted value will be  $\beta = 0.25 \pm 0.05$  m/s. Note that this expression is only valid for a positive extraction velocity, so for a stretched film, at a tension higher than its surrounding meniscus.

As previously discussed, the first moments of the film extraction is not described by this process and an initial film of uniform reference thickness is used as the initial condition. During the dynamics, some new film elements are added in the system, thus increasing the range value for the Lagrangian coordinate  $x$  which varies between  $x = 0$  at the top and

$x = H_0(t)$  at the bottom. The film extraction at the velocity  $U_{Fr}(H_0)$  is associated to the increase of  $H_0$  at the rate

$$\frac{dH_0}{dt} = \frac{U_{Fr}(H_0)}{1 + \epsilon(H_0(t))} \quad (17)$$

The thickness  $h_{Fr}$  of the extracted film elements is governed by Eq. (3) and thus depends on the local deformation  $\epsilon(H_0)$  through Eq. (16). The reference thickness  $h_0$  can then be computed at  $x = H_0(t)$  using Eq. (8)

$$h_0(H_0) = h_{Fr}(U_{Fr}(H_0)) \times (1 + \epsilon(H_0)) \quad (18)$$

The mechanism at the origin of film extraction from the lateral meniscus is the same as the one at the origin of the extraction from the bottom meniscus.

The width of the lateral extracted film  $w_{Fr}$  thus increases at the rate  $\partial_t w_{Fr}(x) = U_{Fr}(x)$  and its area varies as

$$\frac{dA_{Fr}}{dt} = \int_0^{H_0} U_{Fr}(x)(1 + \partial_x \xi) dx \quad (19)$$

With this model the lateral film width  $w_{Fr}(x)$  should be an increasing function of  $x$ , first because the extraction begins sooner at smaller  $x$  (because the film element is created earlier), and second because the tension, and thus the extraction velocity is higher at the top of the film.

We observe experimentally that these lateral films are actually wider in the central part (see Fig. 2). This is due to the fact that they are thicker than the central part of the film, which leads to their fast downward motion. As this dynamical effect is beyond our theoretical description, we choose to take it into account through a phenomenological correction of the model. The area evolution of the lateral extracted film is still the one predicted by Eq. (19), but its shape is assumed to be a rectangle of uniform width  $\bar{w}_{Fr}$  verifying  $H\bar{w}_{Fr} = A_{Fr}$ . This artificial redistribution of the lateral film elements mimics the downward lateral motion in the simplest possible way, and keeps a realistic shape for the central part of the film, which is the system of interest. The central film width is thus assumed to be uniform, with  $w(t) = w_0 - 2\bar{w}_{Fr}$ .

## 4.4 Numerical resolution

### 4.4.1 Equations set

The film profile is determined by its reference thickness  $h_0(x)$  and by its deformation  $\epsilon(x, t)$ . As the model is based on an equilibrium equation, it only evolves because of the boundary conditions evolution: the variation of its width  $w(t)$  and of its reference height  $H_0(t)$ . At each time,  $h_0$  is obtained at the bottom of the film from Eq. (18) and  $w(t)$  is deduced from Eq. (19). The Eq. (15) can thus be numerically integrated if the tension is known at a given point of the film.

The missing information is obtained from the total height of the film, imposed by the motors motion:

$$H(t) = \int_0^{H_0} (1 + \partial_x \xi(x)) dx \quad (20)$$

By using Eq. (13), we can express  $\partial_x \xi(x)$  as a function of  $\epsilon(x)$ , leading to

$$H(t) = \int_0^{H_0} \frac{w_0}{w(x)} (1 + \epsilon(x)) dx \quad (21)$$

Introducing the auxiliary function

$$f(x) = \frac{\epsilon(H_0)}{1 + \epsilon(H_0)} - \frac{\epsilon(x)}{1 + \epsilon(x)} \quad (22)$$

we get, from Eq. (15),

$$f(x) = -\frac{1}{\ell} \int_x^{H_0} \frac{h_0(x)}{h_{00}} \frac{w_0}{w(t)} dx \quad (23)$$

The function  $f$  is thus expressed as a function of the known quantities  $h_0$  and  $w$ . The Eq. (21) leads to

$$H(t) = \int_0^{H_0} \frac{w_0}{w(t)} \frac{1}{1 - f_0 + f(x)} dx, \quad (24)$$

wich provides an implicit equation for the parameter  $f_0 = \epsilon(H_0)/(1 + \epsilon(H_0))$ . Once  $f_0$  has been determined from Eq. (24), the film extension can be deduced from Eq. (22), which closes the model.

The problem can in principle be solved from an initial reference film height  $H_0(0) = 0$ , thus addressing the first moments of the film extraction from the bottom meniscus. However, using our experimental parameters, this model leads to unrealistic prediction for the first 10 cm, and we assume that inertial effects are non-negligible at this stage. We thus initialize the code with a small film of height  $H_0$ , and of uniform thickness  $h_0$  and width  $w_0$ . This initial film corresponds to the liquid entrained by inertia and viscosity at very short time.

#### 4.4.2 Numerical scheme

The numerical resolution of the model was carried out under Python. The film is discretized in  $n$  strips. Their reference height  $dx$  is uniform, except for the bottom strip which has a variable height  $dx^*$ . At each time step, the height  $H$  is increased by  $Vdt$ , with  $V$  the velocity of the motors. We compute  $f(x)$  in each film element *via* Eq. (23). We determine the tension at the bottom meniscus  $\epsilon(H_0)$  (Eq. (22)) by solving Eq. (24) to find the value of  $f_0$ . The tension  $\epsilon(x)$  in each element is deduced from  $f(x)$  using Eq. (22). The thickness  $h(x)$  is computed using Eq. (8). If the tension at the bottom of the film is larger than  $\gamma_0$ , the film length  $dz_{Fr} = U_{Fr} dt$  is extracted from the bottom meniscus. The height of the last element  $dx^*$  is thus increased by

$$dx_{Fr} = \frac{U_{Fr} dt}{1 + \epsilon(H_0)}. \quad (25)$$

and the reference thickness  $h_0(H_0)$  of the last segment is recalculated so that  $h(H_0) = h_{Fr}$  (Eq. (1)) and  $h(H_0) = h_0(H_0)/(1 + \epsilon(H_0))$ . As soon as  $dx^* \geq 2dx$ , the strip  $n$  is divided in two: the strip  $n$  with a reference height  $dx$  and the strip  $n + 1$  with the reference height  $dx^* - dx$ . The height of the film at rest is recalculated as  $H_0 = ndx$ . The increase of the lateral extracted film is computed from Eq. (19). The central film width is then obtained from

$$w = w_0 - 2 \frac{A_{Fr}}{H}. \quad (26)$$

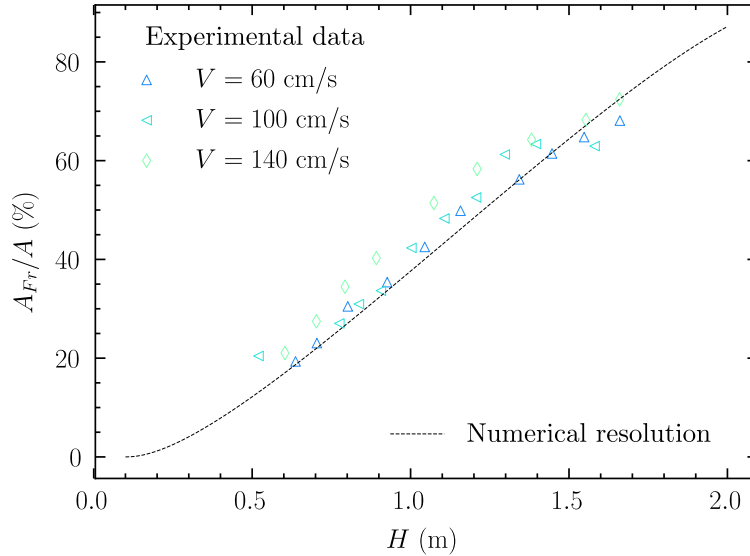


Figure 9: Evolution of the proportion of the area of the lateral Frankel films  $A_{Fr}$  to the total area of the films  $A$  as a function of the height  $H$  reached by the soap films during their generation for three different velocities: 60 cm/s, 100 cm/s and 140 cm/s (data identical to those shown in Fig. 6). The black dashed line is the numerical resolution of the model for  $V = 100$  cm/s and  $\beta = 0.26$  m/s.

## 4.5 Results of the numerical resolution

### 4.5.1 Choice of the numerical parameters

There are only two numerical parameters in the equations set: the characteristic length  $\ell$  and the prefactor  $\beta$  involved in the Frankel's law. Their values, as well as the film profile at short time, have been determined from the experimental data, as discussed below.

The experimental profiles are exponential in the initial film, with a characteristic length (Fig. 5)  $\ell = 0.80 \pm 0.09$  m identical for all the velocities. This implies that the reference thickness

$$h_{00} = \frac{2E}{\rho g \ell} \quad (27)$$

is uniform and independent of the motors' velocity.

Using the experimental value of  $\ell$  and  $E = 22$  mN/m [Kim and Mandre, 2017], we obtain that  $h_{00} \simeq 5.6 \mu\text{m}$ . We initiate the numerical simulation with a film of reference height  $H_0 = 10$  cm, and a reference thickness  $h_0 = h_{00} = 5.6 \mu\text{m}$ . The motors' velocity implemented in the simulations is  $V = 100$  cm/s. As discussed before, we used the parameter  $\beta$  in

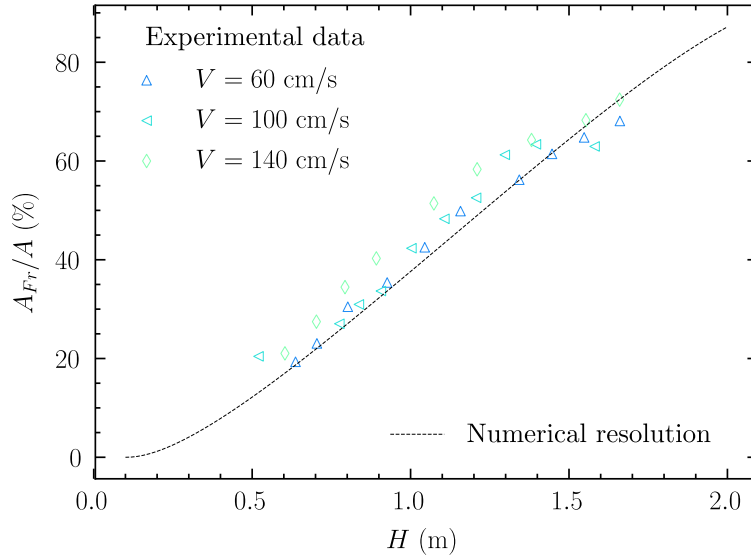


Figure 10: Evolution of the proportion of the area of the lateral Frankel films  $A_{Fr}$  to the total area of the films  $A$  as a function of the height  $H$  reached by the soap films during their generation for three different velocities: 60 cm/s, 100 cm/s and 140 cm/s (data identical to those shown in Fig. 6). The black dashed line is the numerical resolution of the model for  $V = 100$  cm/s and  $\beta = 0.26$  m/s.

Eq. (16) as an adjustable parameter. Its value is determined from the experimental data shown in Fig. 10: the proportion of the Frankel film area as a function of time obtained numerically fits the data for  $\beta = 0.26$  m/s. This value is ten times lower than the one expected if the surface tension in the menisci was equal to that of the bath, which indicates that the lateral menisci are at a tension much higher than the equilibrium tension and that they are depleted in surfactants.

### 4.5.2 Numerical results

The numerical results allow us to quantify the various processes involved in the dynamics. We will first discuss the properties of the initial film, which can be easily followed at different times, using our Lagrangian formalism. A salient feature is the competition between the film extension, due to the motors' motion, and the film extraction, which mitigates this extension. This competition is clearly illustrated by the initial film area, plotted in Fig. 11 as a function of time: it increases during the first second, remaining close to the total film area imposed by the motors' motion, and decreases at longer time, as the Frankel films are invading the films. The largest part of the extraction occurs in the lateral menisci, and the total area of the central film remains close to the area of the initial film.

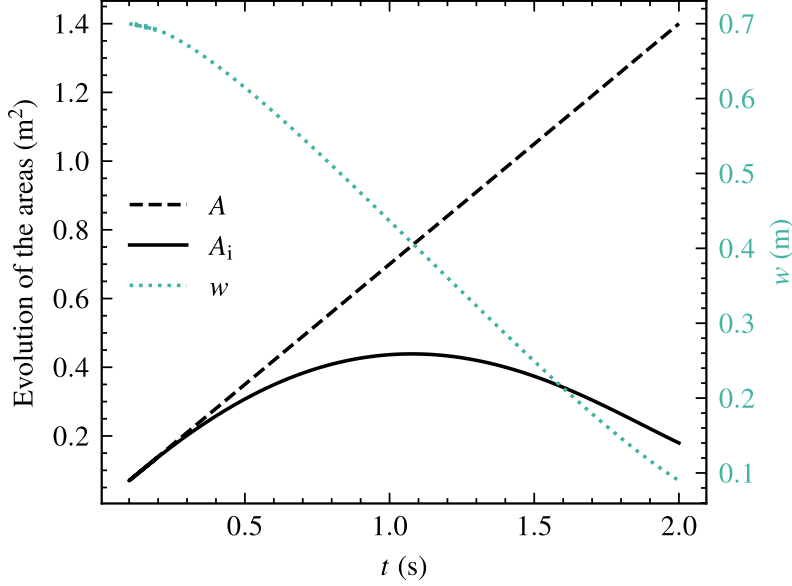


Figure 11: (Left) Evolution of the areas of the initial film  $A_i$  (solid black line) and of the total film area  $A$  (dashed black line) and (Right) evolution of the width  $w$  (dotted green line) as a function of time, obtained numerically.

This non-monotonic evolution is also visible in Fig. 12 (a), where the film extension is plotted as a function of  $z$  for different times. The slope discontinuity in the curves corresponds to the boundary between the initial film and the film extracted from the bottom meniscus.

In the initial film, the average extension is related to the total area of the initial film, whereas the extension gradient is due to gravity. The film tension shown in Fig. 12 (b) is directly deduced from the film extension, using Eq. (7), and governs the film extraction. Its value at the different heights in the film is a complex interplay between (i) the non-monotonic evolution of the mean tension, due to the motors motion and the film extraction, and (ii) the increase of the tension difference between the top and the bottom of the initial film due to the gravity and to the increase of the initial film height. The resulting tension profile leads to the extraction rate from the lateral menisci plotted in Fig. 12 (c): the higher we are in the film, the higher the tension and thus the higher the extraction velocity. It can be noted that, as we will explain later, when the extension values are negative, we have chosen to set a zero extraction velocity at the bottom, and thus prevent the film from entering the bath meniscus. This explains the plateaus observed at long times in Fig. 12 (b,c).

The thickness profile of the initial film is the most important prediction, as it can be compared to the experimental data. Its dimensionless value  $\hat{h} = h/h_{00}$  is plotted using two representations in Fig. 12 (d,e). In Fig. 12 (d), we use the Lagrangian parameter  $x$  so that a given piece of film can be followed during its motion and deformation. At each place in the initial film the non-monotonic behavior is observed, with a thinning followed by a thickening, but the transition occurs at a longer time at the top of the film. The profile is plotted as a function of the actual position in the film  $z$ , in Fig. 12 (e), and the exponential profile is recovered. This profile is a direct consequence of the initial condition we used: as a uniform reference thickness is imposed in the initial film, the profile remains exponential at all times. The prefactor is, however, an important prediction of the model, and shows again, a non-monotonic evolution.

All the results discussed above help describing the physics of the initial film evolution during the motors motion. In Fig. 12 (f), we have represented the thickness profile of the whole central film (the initial film and the film extracted at the bottom at longer times). The transition leads to a non-physical discontinuous film thickness, due to the fact that the initial film thickness has been chosen at the measured value, and the extracted film thickness is imposed by the dynamics. As the tension gradient is governed by the film thickness, the thickness discontinuity leads to the slope discontinuity observed in Fig. 12 (a) (extension). The model leads to compression at the bottom of the film, and to a tension lower than the equilibrium one. This corresponds to a tendency of the system to extract film at the top at high tension, and to absorb some film at the bottom meniscus, where the film tension is lower. Such film absorption is difficult to evidence experimentally, and could be associated with the marginal regeneration observed at the bottom of vertical soap films [Gros et al., 2021]. However, the extraction velocity has been set to zero in that case in order to keep the model simple.

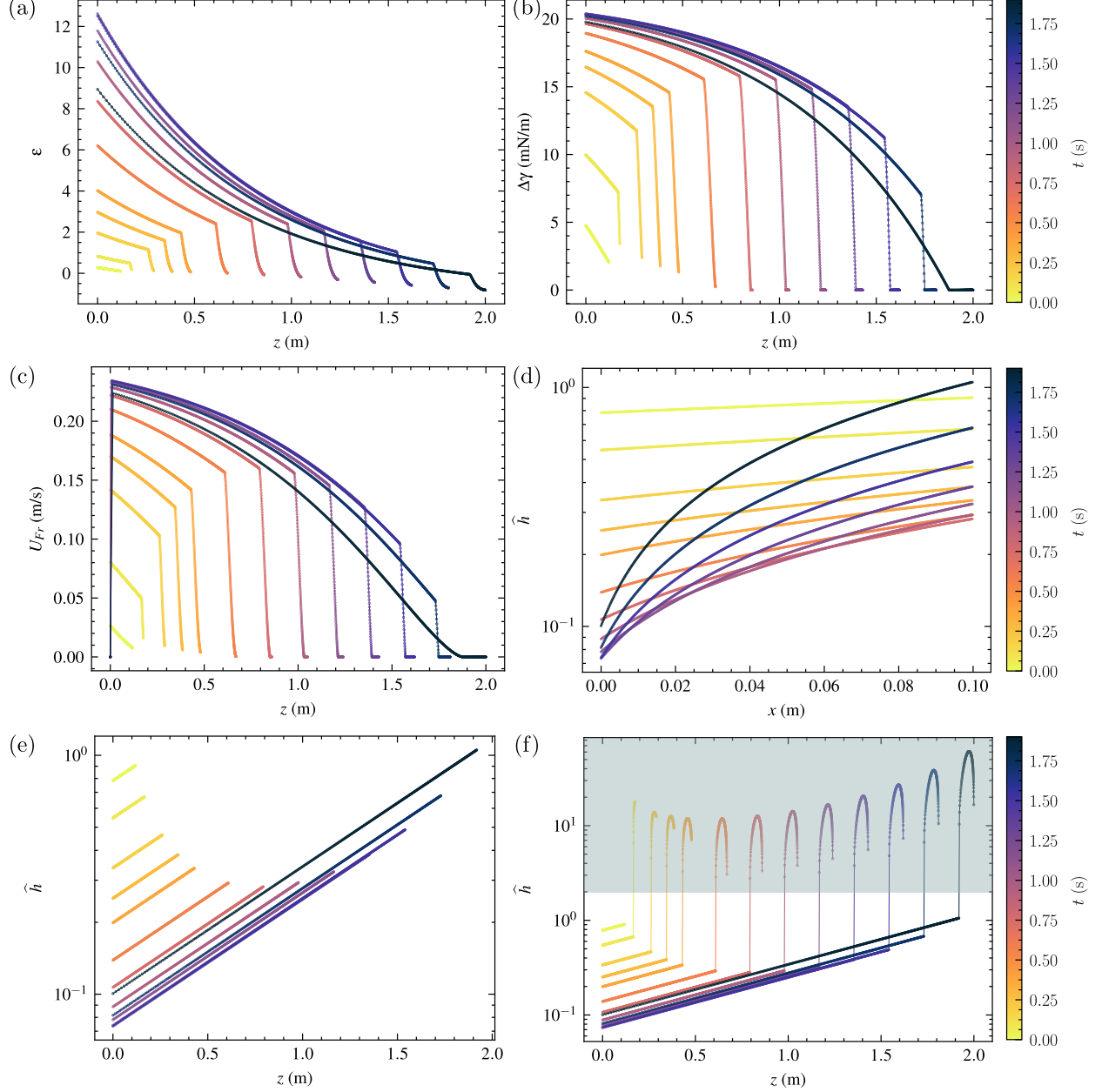


Figure 12: Numerical resolution results for the generation of a film of a width  $w_0 = 70$  cm and an initial height for the reference state  $H_0 = 10$  cm, at a velocity  $V = 100$  cm/s. Each color corresponds to a different time  $t$ , indicated by the vertical color bar. The difference between two represented instants is  $\Delta t = 0.19$  s. (see next page)

## 5 Comparison with experimental data

We propose in this part to compare the results of the numerical resolution presented in the previous section with the experimental results presented in the section 3.3.

In Fig. 13, we have plotted two thickness profiles obtained numerically and experimentally for a film generated at a velocity fixed at 100 cm/s. A good agreement is obtained for the initial film profile. Note that the characteristic length has been fitted on the experimental data, but the prefactor of the exponential profile is quantitatively predicted, which is an important validation of the model.



Figure 12 (previous page): Evolution of (a) the extension  $\epsilon$  as a function of the  $z$  coordinate, (b) the tension  $\Delta\gamma = \gamma - \gamma_0$  as a function of the  $z$  coordinate, (c) the extraction velocity of the lateral Frankel films  $U_{\text{Fr}}$  as a function of the  $z$  coordinate, (d) the dimensionless thickness  $\hat{h} = h/h_{00}$  for the initial film as a function of the  $x$  coordinate, (e) the dimensionless thickness  $\hat{h}$  for the initial film as a function of the  $z$  coordinate, (f) the dimensionless thickness  $\hat{h}$  as a function of the  $z$  coordinate for the whole film: the initial stretched film (whose data are represented in the figure (e)) and the Frankels films extracted from the meniscus with the bath. The circles correspond to the points measured in each element. These resolutions are conducted by dividing the initial film into  $n = 500$  elements and setting the time step  $dt = 10^{-4}$  s.

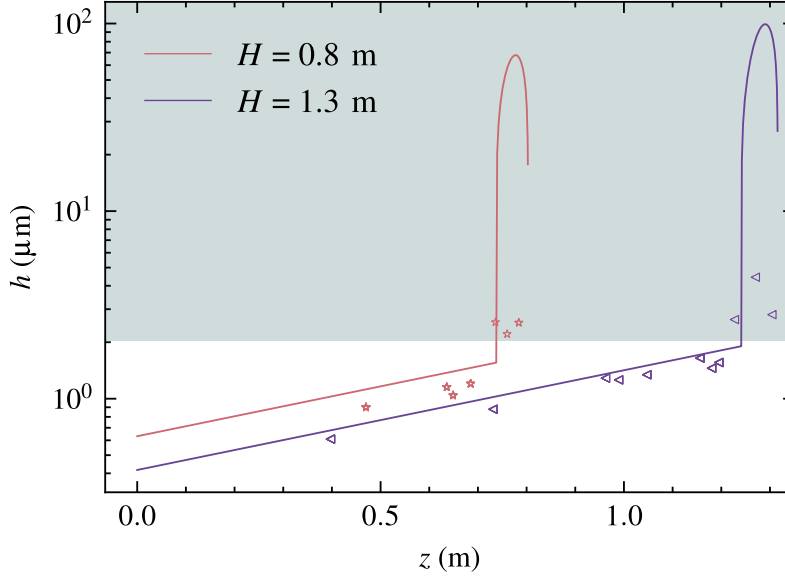


Figure 13: Evolution of the thickness  $h$  as a function of  $z$ , in semi-logarithmic scale, for an entrained velocity fixed at 100 cm/s and two different heights:  $H = 0.8$  m (pink) and  $H = 1.3$  m (purple). The solid line corresponds to the numerical resolution while the points (triangles or stars) are experimental data identical to those in Fig. 5.

In the film extracted at the bottom, the thickness obtained numerically is more than 10 times larger than the experimental one, which is a failure of the model. This may be due to the fact that we did not take into account the Poiseuille flow induced by gravity. Indeed, the downwards Poiseuille flow scales as  $\rho gh^2/\eta$ . Thus, for thicknesses between 10 and 100  $\mu\text{m}$  gravity become non-negligible in the extracted film ( $\rho gh^2/\eta \sim 0.1 - 10$  cm/s). This explains that the measured thicknesses are smaller than the prediction. However, the width of this film is reasonably captured.

Importantly, the dynamics of the initial film, on which this paper focuses, is not affected by this non-physical film thickness at the bottom. The tension profile in the initial film is governed by the gravity and by the constraint that the initial film must reach a total height, determined by the top wire position and by the location of the boundary with the extracted film at the bottom. Only the size of the bottom extracted film matters for the initial film dynamics, not its thickness. As the bottom extracted film has a negligible size, both experimentally and numerically, the prediction made for the initial film are independent of this extraction at the bottom. The only consequence of the overestimated film thickness is the strong decrease of the tension, which reaches non-physical small values at the bottom meniscus.

In the following, we restrict the analysis to the initial film. The experimental and numerical film profiles are fitted by the exponential shape  $Ke^{(z-H)/\ell}$ , and the obtained values of the prefactor  $K$  are compared. They are plotted as a function of the film height in Fig. 14 (a). Over the range of heights we can access in our experiment, between 0.5 and 1.9 m, the values of  $K$  predicted by the numerical resolution are in agreement with our data. However, a discrepancy can be noticed when the height of the films becomes close to 2 m. This may be related to our method of redistributing the films in rectangular form, which becomes too far from the redistribution actually observed experimentally for the highest films.

This observation is confirmed if we compare the measurements directly made by spectrometry, for example at 30 cm above the bath, with the numerical resolution. Indeed, in Fig. 14 (b), we observe a good qualitative agreement between

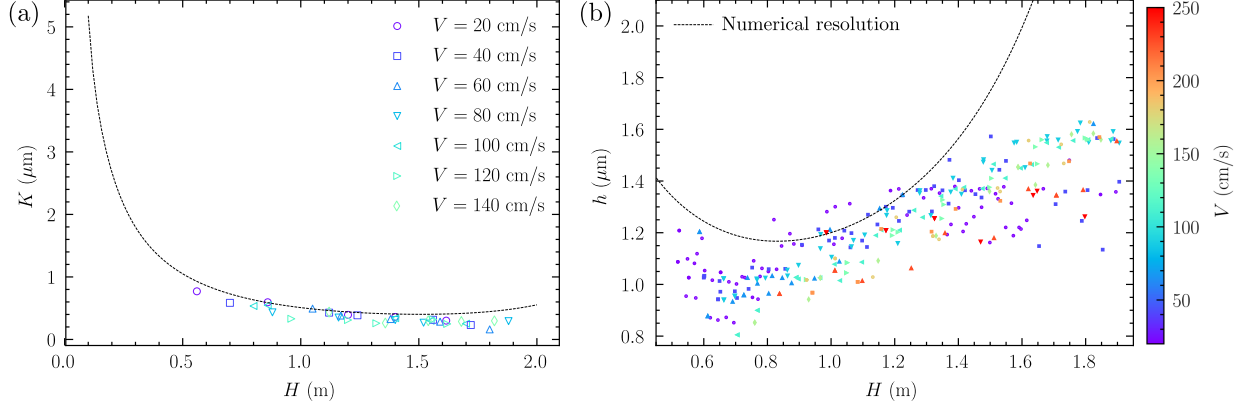


Figure 14: (a) Comparison between the prefactor of the exponential profiles  $K$  of the films measured experimentally for different velocities (ranging from 20 cm/s to 140 cm/s) and the one determined using the numerical resolution (black dashed line). The values of  $K$  are plotted as a function of the height reached by the soap films  $H$  during the generation. (b) Evolution of the thickness  $h$  of the soap films during generation as a function of the height  $H$  reached by the films for all velocities probed between 20 cm/s and 250 cm/s. The colored points correspond to measurements taken at 30 cm above the liquid bath. These data are identical to those shown in the Fig. 4 (b). The black dotted line corresponds to the evolution of  $h$  given by the numerical resolution.

the model and the experiment. First a decrease of the thickness is noted, then a minimum value is obtained at a similar height of film, and finally a thickening is observed. However, this thickening is much faster than the increase in thickness measured experimentally.

## 6 Conclusion

The aim of this article is to describe the thickness profile of giant foam films during their generation. Our main result is the successful description of the thickness profile in the central part of the film. This necessitated a phenomenological description of the extraction of thick film from the lateral and bottom menisci. Our current understanding of these foam films generation is summarized below.

At short time, the liquid is entrained by viscosity around the wire, as it would be the case with a much more viscous liquid, like silicon oil [Champougny et al., 2017]. A reasonable hypothesis is that the reference state is prescribed by the moment at which this viscous flow is counterbalanced by the apparition of a strong enough Marangoni stress allowing entering the regime described in this article.

This initial film is then stretched and we have shown that its shape is an exponential profile predicted the hydrostatic model. This is true though the pulling velocities are large, up to meters per seconds. Additionally, the characteristic length of the exponential depends neither on the pulling velocity nor on the time. This is a strong indication that an equilibrium shape of the film exists with a reference thickness  $h_0$  and a reference area  $A_0$ . What fixes this reference remains unknown.

We show that the relaxation of the central films starts during the generation and is governed by the extraction of thicker film from the lateral menisci. The extraction law we use in the model is nevertheless not quantitative. As explained in the text, this can be due to the fact that we do not know the value of the surface tension in the menisci.

Finally, when the motors stop, we expect a competition between the relaxation of the central film due to further extraction of thick films from the lateral meniscus and a thinning due to both drainage and evaporation. A quantitative description of these mechanisms would be necessary to predict the lifetime of the soap film.

## Acknowledgments

We are grateful to François Boulogne for the design of the Oospectro library, and Vincent Klein and Sandrine Mariot for the design of the experimental setup. Funding from ESA (MAP Soft Matter Dynamics) and CNES (through the GDR MFA) is acknowledged. IC has received funding from the European Research Council (ERC) under the European Union's Horizon 2020 research and innovation program (grant agreement No 725094).

## References

- Graeme Denton. Tallest free-standing soap bubble, 2020. URL <https://www.guinnessworldrecords.com/world-records/584518-tallest-free-standing-soap-bubble>.
- P Ballet and F Graner. Giant soap curtains for public presentations. *European Journal of Physics*, 27(4):951–967, jun 2006. doi:10.1088/0143-0807/27/4/026.
- Hamid Kellay and Walter I Goldburg. Two-dimensional turbulence: a review of some recent experiments. *Reports on Progress in Physics*, 65(5):845–894, apr 2002. doi:10.1088/0034-4885/65/5/204.
- H. Kellay. Hydrodynamics experiments with soap films and soap bubbles: A short review of recent experiments. *Physics of Fluids*, 29(11):111113, 2017. doi:10.1063/1.4986003.
- M. A. Rutgers, X. L. Wu, and W. B. Daniel. Conducting fluid dynamics experiments with vertically falling soap films. *Review of Scientific Instruments*, 72(7):3025–3037, 2001. doi:10.1063/1.1379956.
- Aakash Sane, Shreyas Mandre, and Ildoo Kim. Surface tension of flowing soap films. *Journal of Fluid Mechanics*, 841: R2, 2018. doi:10.1017/jfm.2018.28.
- Louis Salkin, Alexandre Schmit, Pascal Panizza, and Laurent Courbin. Generating soap bubbles by blowing on soap films. *Phys. Rev. Lett.*, 116:077801, Feb 2016. doi:10.1103/PhysRevLett.116.077801.
- Ildoo Kim and Shreyas Mandre. Marangoni elasticity of flowing soap films. *Phys. Rev. Fluids*, 2:082001, Aug 2017. doi:10.1103/PhysRevFluids.2.082001.
- Sandrine Mariot, Marina Pasquet, Vincent Klein, Frédéric Restagno, and Emmanuelle Rio. A new setup for giant soap films characterization. *The European Physical Journal E*, 44(4):1–8, 2021.
- Sylvie Lioni-Addad and Jean Marc Di Meglio. Stabilization of aqueous foam by hydrosoluble polymers. 1. sodium dodecyl sulfate-poly(ethylene oxide) system. *Langmuir*, 8(1):324–327, 1992. doi:10.1021/la00037a059.
- Sylvie Cohen-Addad and Jean-Marc di Meglio. Stabilization of aqueous foam by hydrosoluble polymers. 2. role of polymer/surfactant interactions. *Langmuir*, 10(3):773–778, 1994. doi:10.1021/la00015a029.
- Eric A. Adelizzi and Sandra M. Troian. Interfacial slip in entrained soap films containing associating hydrosoluble polymer. *Langmuir*, 20(18):7482–7492, 2004. doi:10.1021/la035480x. PMID: 15323492.
- Steffen Berg, Eric A. Adelizzi, and Sandra M. Troian. Experimental study of entrainment and drainage flows in microscale soap films. *Langmuir*, 21(9):3867–3876, 2005. doi:10.1021/la047178+. PMID: 15835948.
- Laurie Saulnier, Frédéric Restagno, Jérôme Delacotte, Dominique Langevin, and Emmanuelle Rio. What is the mechanism of soap film entrainment? *Langmuir*, 27(22):13406–13409, 2011. doi:10.1021/la202233f. PMID: 22004182.
- Laurie Saulnier, Lorène Champougny, Gaël Bastien, Frédéric Restagno, Dominique Langevin, and Emmanuelle Rio. A study of generation and rupture of soap films. *Soft Matter*, 10:2899–2906, 2014. doi:10.1039/C3SM52433G.
- Jacopo Seiwert, Ronan Kervil, Soniraks Nou, and Isabelle Cantat. Velocity field in a vertical foam film. *Phys. Rev. Lett.*, 118:048001, Jan 2017. doi:10.1103/PhysRevLett.118.048001.
- Lorène Champougny, Jonas Miguët, Robin Henaff, Frédéric Restagno, Francois Boulogne, and Emmanuelle Rio. Influence of evaporation on soap film rupture. *Langmuir*, 34(10):3221–3227, 2018. doi:10.1021/acs.langmuir.7b04235. PMID: 29498527.
- KJ Mysels, K. Shinoda, and S. Frankel. *Soap Films: Studies of their Thinning and a Bibliography*. Pergamon, New York, 1959.
- Jacopo Seiwert, Benjamin Dollet, and Isabelle Cantat. Theoretical study of the generation of soap films: role of interfacial visco-elasticity. *Journal of fluid mechanics*, 739:124–142, 2014a.
- Lorène Champougny, Benoit Scheid, Frédéric Restagno, Jan Vermant, and Emmanuelle Rio. Surfactant-induced rigidity of interfaces: a unified approach to free and dip-coated films. *Soft matter*, 11(14):2758–2770, 2015.
- J Willard Gibbs. *The collected works of J. Willard Gibbs*. Longmans, Green and Co., 1928.
- A Prins, C Arcuri, and M Van den Tempel. Elasticity of thin liquid films. *Journal of Colloid and Interface Science*, 24(1):84–90, May 1967. ISSN 00219797. doi:10.1016/0021-9797(67)90281-0.
- Isabelle Cantat. Liquid meniscus friction on a wet plate: Bubbles, lamellae, and foams. *Physics of Fluids*, 25(3): 031303, 2013. doi:10.1063/1.4793544.
- Jacopo Seiwert, Benjamin Dollet, and Isabelle Cantat. Theoretical study of the generation of soap films: role of interfacial visco-elasticity. *Journal of Fluid Mechanics*, 739:124–142, 2014b. doi:10.1017/jfm.2013.625. URL <http://dx.doi.org/10.1017/jfm.2013.625>.

- E.H. Lucassen-Reynders. Anionic surfactants: Physical chemistry of surfactant action, chapter 6. Surfactant science series. M. Dekker, 1981.
- Yves Couder. The observation of a shear flow instability in a rotating system with a soap membrane. J. Physique Lett., 42:429 – 431, Oct 1981. doi:10.1051/jphyslet:019810042019042900.
- Pierre-Gilles de Gennes. “young” soap films. Langmuir, 17(8):2416–2419, 2001.
- N Adami and H Caps. Surface tension profiles in vertical soap films. Physical Review E, 91(1):13007, 2015.
- M. Van den Tempel, J. Lucassen, and E. H. Lucassen-Reynders. Application of Surface Thermodynamics to Gibbs Elasticity. The Journal of Physical Chemistry, 69(6):1798–1804, June 1965. ISSN 0022-3654, 1541-5740. doi:10.1021/j100890a002.
- M. A. Rutgers, X. I. Wu, R. Bhagavatula, A. A. Petersen, and W. I. Goldburg. Two-dimensional velocity profiles and laminar boundary layers in flowing soap films. 8(11):2847–2854, 1996. doi:10.1063/1.869105.
- Paul Stevenson. Remarks on the shear viscosity of surfaces stabilised with soluble surfactants. Journal of Colloid and Interface Science, 290(2):603–606, 2005. ISSN 0021-9797. doi:https://doi.org/10.1016/j.jcis.2005.07.070. URL <https://www.sciencedirect.com/science/article/pii/S0021979705008404>.
- Alice Gros, Adrien Bussonnière, Sanjiban Nath, and Isabelle Cantat. Marginal regeneration in a horizontal film: Instability growth law in the nonlinear regime. Phys. Rev. Fluids, 6(2):024004, 2021.
- Lorène Champougny, Emmanuelle Rio, Frédéric Restagno, and Benoit Scheid. The break-up of free films pulled out of a pure liquid bath. Journal of fluid mechanics, 811:499–524, 2017.